Numerical Analysis of Large-Diameter Monopiles in Dense Sand Supporting Offshore Wind Turbines

Sheikh Sharif Ahmed[1] and Bipul Hawlader[2]

[1]Department of Civil Engineering, Memorial University of Newfoundland, St. John's, Newfoundland, Canada A1B 3X5
Tel: +1 (709) 864-8920, E-mail: ssa725@mun.ca

[2]**Corresponding Author:** Associate Professor, Department of Civil Engineering, Memorial University of Newfoundland, St. John's, Newfoundland, Canada A1B 3X5
Tel: +1 (709) 864-8945 Fax: +1 (709) 864-4042 E-mail: bipul@mun.ca

Abstract

Large-diameter monopiles are widely used foundations for offshore wind turbines. In the present study, three-dimensional finite element (FE) analyses are performed to estimate the static lateral load-carrying capacity of monopiles in dense sand subjected to eccentric loading. A modified Mohr-Coulomb (MMC) model that considers the pre-peak hardening, post-peak softening and the effects of mean effective stress and relative density on stress–strain behavior of dense sand is adopted in the FE analysis. FE analyses are also performed with the Mohr-Coulomb (MC) model. The load–displacement behavior observed in model tests can be simulated better with the MMC model than the MC model. Based on a parametric study for different length-to-diameter ratio of the pile, a load–moment capacity interaction diagram is developed for different degrees of rotation. A simplified model, based on the concept of lateral pressure distribution on the pile, is also proposed for estimation of its capacity.

Keywords: monopiles; finite element; dense sand; modified Mohr-Coulomb model; lateral load; offshore wind turbine.

Introduction

Wind energy is one of the most promising and fastest growing renewable energy sources around the world. Because of steady and strong wind in offshore environments as compared to onshore, along with less visual impact, a large number of offshore wind farms have been constructed and are under construction. The most widely used foundation system for offshore wind turbines is the monopile, which is a large-diameter 3–6 m hollow steel driven pile having length-to-diameter ratio less than 8 (e.g., LeBlanc et al. 2010; Doherty and Gavin 2012; Doherty et al. 2012; Kuo et al. 2011). Monopiles have been reported to be an efficient solution for offshore wind turbine foundations in water depth up to 35 m (Doherty and Gavin 2012). The dominating load on offshore monopile is the lateral load from wind and waves, which acts at a large eccentricity above the pile head.

To estimate the load-carrying capacity of monopiles, the *p*–*y* curve method recommended by the American Petroleum Institute (API 2011) and Det Norske Veritas (DNV 2011) are widely used. A *p*–*y* curve defines the relationship between mobilized soil resistance (*p*) and the lateral displacement (*y*) of a section of the pile. The reliability of the *p*–*y* curve method in monopile design has been questioned by a number of researchers (e.g., Abdel-Rahman and Achmus 2005; Lesny and Wiemann 2006; Achmus et al. 2009; LeBlanc et al. 2010; Doherty and Gavin 2012). The API and DNV recommendations are slightly modified form of the *p*–*y* curve method proposed by Reese et al. (1974) mainly based on field tests results of two 610 mm diameter flexible slender piles. However, the large-diameter offshore monopiles behave as a rigid pile under lateral loading. Moreover, in the API recommendations, the initial stiffness of the *p*–*y* curve is independent of the diameter of the pile, which is also questionable. Doherty and Gavin (2012) discussed the limitations of the API and DNV methods to calculate the lateral load-carrying capacity of offshore monopiles.

Monopiles have been successfully installed in a variety of soil conditions; however, the focus of the present study is to model monopiles in dense sand. Studies have been performed in the past for both static and cyclic loading conditions (e.g., Achmus et al. 2009; Cuéllar 2011; Ebin 2012); however, cyclic loading is not discussed further because it is not the focus of the present study. To understand the behavior of large-diameter monopiles in sand, mainly three different approaches have been taken in recent years, namely physical modeling, numerical modeling, and modification of the *p*–*y* curves. LeBlanc et al. (2010) reported the response of a small-scale model pile under static and cyclic loading installed in loose and dense sand. Centrifuge tests were also conducted in the past to understand the response of large-diameter monopiles in dense sand subjected to static and cyclic lateral loading at different eccentricities (e.g., Klinkvort et al. 2010; Klinkvort and Hededal 2011; Klinkvort and Hededal 2014). Møller and Christiansen (2011) conducted 1g model tests in saturated and dry dense sand. Conducting centrifuge tests using 2.2 m and 4.4 m diameter monopiles, Alderlieste (2011) showed that the stiffness of the load–displacement curves increases with diameter. The comparison of results of centrifuge tests and the API approach shows that the API approach significantly overestimates the initial stiffness of the load–displacement behavior. In order to match test data, Alderlieste (2011) modified the API formulation by introducing a stress-dependent stiffness relation. However, the author recognized that the modified API approach still underestimates the load at small displacements and overestimates at large displacements and therefore recommended for further studies. It is also to be noted here that, small-scale model tests were conducted in the past to estimate the lateral load-carrying capacity of rigid piles and bucket foundations (e.g., Prasad and Chari 1999; Lee et al. 2003; Ibsen et al. 2014). However, contradictory evidences of diameter effects warrant further investigations from a more fundamental understanding (Doherty and Gavin 2012).

Finite element modeling could be used to examine the response of monopiles under eccentric loading. In the literature, FE modeling of large-diameter monopiles is limited as compared to slender piles. Most of the previous FE analyses were conducted mainly using Plaxis 3D and Abaqus FE software. The back-calculated *p*–*y* curves from FE results show that the API recommendations significantly overestimates the initial stiffness (Hearn and Edgers 2010; Møller and Christiansen 2011). Overestimation of the ultimate resistance in FE simulation, as compared to model test results, has been also reported in previous study (Møller and Christiansen 2011). FE modeling also shows that the soil model has a significant influence on load–displacement behavior of monopile (Wolf et al. 2013).

Most of the above FE analyses have been conducted using the built-in Mohr-Coulomb (MC) model. In commercial FE software (e.g., Abaqus), the angle of internal friction and dilation angle are defined as input parameters for the MC model. However, laboratory tests on dense sands show post-peak softening behavior with shear strain, which should be considered in numerical modeling for a better understanding of the response of monopiles in dense sand.

The objective of the present study is to conduct FE modeling of monopile foundations for offshore wind turbines under static lateral loading. A realistic model that captures the key features of stress–strain behavior of dense sand is adopted in the FE modeling, which could explain the load–displacement behavior observed in model tests. A simplified method is also proposed for preliminary estimation of load-carrying capacity of monopile.

Finite element model

A monopile of length *L* and diameter *D* installed in dense sand is simulated in this study. During installation, the soil surrounding the monopile can be disturbed. However, the effects of disturbance on the capacity are not considered in this study, instead the simulations are performed for a wished-in-place monopile. The monopile is laterally loaded for different load eccentricities as shown in Fig. 1(a). Analyses are also performed only for pure moment applied to the pile head. The sign convention used for displacement and rotation of the monopile is also shown in Fig. 1(a). Figure 1(b) shows an idealized horizontal stress distribution on the pile. Figure 1(c) shows the loading conditions of the soil elements around the pile. Further discussion on Figs. 1(b) and 1(c) are provided in the following sections.

The FE analyses are performed using Abaqus/Explicit (Abaqus 6.13-1) FE software. Pile–soil interactions are investigated by modeling the buried section of the monopile and surrounding soil. Taking the advantage of symmetry, only a half-circular soil domain of diameter 15*D* and depth 1.67*L* is modeled (Fig. 2a). The soil domain shown in Fig. 2(a) is large enough compared to the size of the monopile; and therefore, significant boundary effects are not expected on calculated load, displacement and soil deformation mechanisms; which have been also verified by conducting analyses with larger soil domains. The vertical plane of symmetry is restrained from any displacement perpendicular to it, while the curved vertical sides of the soil domain are restrained from any lateral displacement using roller supports at the nodes. The bottom boundary is restrained from any vertical displacement, while the top boundary is free to displace. The soil is modeled using the C3D8R solid homogeneous elements available in Abaqus/Explicit element library, which is an 8-node linear brick element with reduced integration and hourglass control. Typical FE mesh used in this study is shown in Fig. 2(a), which is selected based on a mesh sensitivity analysis. The pile is modeled as a rigid body. The reference point of the rigid pile, located at a distance e above the pile head on the centerline of the pile, is displaced laterally along the X direction. The reaction force in the X direction at the reference node represents the lateral force (H), which generates a lateral load (H) and moment M ($=H\times e$) at the pile head (Fig. 1b). For the pure moment cases, only a moment M is applied to the pile head without H by applying a rotation at the reference point located at the pile head (i.e. e=0).

Modeling of the monopile

The pile–soil interaction behavior is significantly influenced by the rigidity of pile (e.g., Dobry et al. 1982; Briaud et al. 1983; Budhu and Davies 1987; Carter and Kulhawy 1988). To characterize rigid or flexible behavior, Poulos and Hull (1989) used a rigidity parameter, $R=(E_pI_p/E_s)^{0.25}$, where I_p is the moment of inertia of the pile, E_p and E_s are the Young's modulus of the pile and soil, respectively. They also suggested that if $L\leq1.48R$ the pile behaves as rigid while it behaves as a flexible pile if $L\geq4.44R$. Monopiles used for offshore wind turbine foundations generally behave as a rigid pile (LeBlanc et al. 2010; Doherty and Gavin 2012).

Therefore, all the analysis presented in the following sections, the pile is modeled as a rigid body because it saves the computational time significantly.

Modeling of sand

The elastic perfectly plastic Mohr-Coulomb (MC) model has been used in the past to evaluate the performance of monopile foundations in sand (e.g., Abdel-Rahman and Achmus 2006; Sørensen et al. 2009; Achmus et al. 2009; Kuo et al. 2011; Wolf et al. 2013). However, the Mohr-Coulomb model has some inherent limitations. Once a soil element reaches the yield stress, which is defined by the Mohr-Coulomb failure criterion, constant dilation is employed which implies that dense sand will continue to dilate with shearing, whereas laboratory tests on dense sands show that the dilation angle gradually decreases to zero with plastic shearing and the soil element reaches the critical state. In the present study, this limitation is overcome by employing a modified form of Mohr-Coulomb (MMC) model proposed by Roy et al. (2014, 2015) which takes into account the effects of pre-peak hardening, post-peak softening, density and confining pressure on mobilized angle of internal friction (ϕ') and dilation angle (ψ) of dense sand. A summary of the constitutive relationships of the MMC model is shown in Table 1. Figure 2(b) shows the typical variation of mobilized ϕ' and ψ with plastic shear strain (γ^p). The following are the key features of the MMC model.

The peak friction angle (ϕ'_p) increases with relative density but decreases with confining pressure, which is a well-recognized phenomena observed in triaxial and direct simple shear (DSS) tests (e.g., Bolton 1986; Tatsuoka et al. 1986; Hsu and Liao 1998; Houlsby 1991; Schanz and Vermeer 1996; Lings and Dietz 2004). Mathematical functions for mobilized ϕ' and ψ with plastic shear strain, relative density and confining pressure have been proposed in the past (Vermeer and deBorst 1984; Tatsuoka et al. 1993; Hsu and Liao 1998; Hsu 2005). Reanalyzing additional laboratory test data, Roy et al. (2014, 2015) proposed the improved relationships shown in Table 1 (MMC model) and used for successful simulation of pipeline–soil interaction behavior. Further details of the model and parameter selection are discussed in Roy et al. (2014a, b) and are not repeated here.

In Abaqus, the proposed MMC model cannot be used directly using any built-in model; therefore, in this study it is implemented by developing a user subroutine VUSDFLD written in FORTRAN. In the subroutine, the stress and strain components are called in each time increment and from the stress components the mean stress (p') is calculated. The value of p' at the initial condition represents the confining pressure (σ'_c), which is stored as a field variable to calculate Q (see the equation in the first row of Table 1). Using the strain increment components, the plastic shear strain increment $\dot{\gamma}^p$ is calculated as $\sqrt{3(\dot{\epsilon}^p_{ij}\dot{\epsilon}^p_{ji})/2}$ for triaxial configuration, where $\dot{\epsilon}^p_{ij}$ is the plastic strain increment tensor. The value of γ^p is calculated as the sum of $\dot{\gamma}^p$ over the period of analysis. In the subroutine, γ^p and $p'$are defined as two field variables FV1 and FV2, respectively. In the input file, using the equations shown in Table 1, the mobilized ϕ' and ψ are defined in tabular form as a function of γ^p and p'. During the analysis, the program accesses the subroutine and updates the values of ϕ' and ψ with field variables.

Model parameters

The soil parameters used in the FE analyses are listed in Table 2. As shown in Fig. 1(c), the mode of shearing of a soil element around the monopile depends on its location. For example, in Fig. 1(c), the loading on soil element A is similar to triaxial compression, while the elements B and C are loaded similar to DSS condition. Experimental results show that the parameters A_ψ and k_ψ that define peak friction (ϕ'_p) and dilation angle (ψ_p) (i.e. 2nd and 3rd Eqs.

in Table 1) depend on the mode of shearing (e.g., Bolton 1986; Houlsby 1991; Schanz and Vermeer 1996). For example, Bolton (1986) recommended A_ψ=5 and k_ψ=0.8 for plane strain condition and A_ψ=3 and k_ψ=0.5 for triaxial condition. In a recent study, Chakraborty and Salgado (2010) showed that A_ψ=3.8 and k_ψ=0.6 is valid for both triaxial and plane strain condition for Toyoura sand. The soil around the pile under eccentric loading is not only in triaxial or plane strain condition but varies in a wide range of stress conditions depending upon depth (z) and α (Figs. 1b, c). Therefore, in this study A_ψ=3.8 and k_ψ=0.6 is used for simplicity. In addition, based on Chakraborty and Salgado, (2010), the parameter Q is varied as $Q=7.4+0.6\ln(\sigma_c')$ with $7.4 \leq Q \leq 10$.

The interaction between pile and surrounding soil is modeled using the Coulomb friction model, which defines the friction coefficient (μ) as $\mu=\tan(\phi_\mu)$, where ϕ_μ is the soil–pile interface friction angle. The value of ϕ_μ/ϕ' varies between 0 and 1 depending upon the surface roughness, mean particle size of sand and the method of installation (CFEM 2006; Tiwari et al. 2010). For smooth steel pipe piles, ϕ_μ/ϕ is in the range of 0.5–0.7 (Potyondy 1961; Coduto 2001; Tiwari and Al-Adhadh 2014). For numerical modeling, ϕ_μ/ϕ' within this range has been also used in the past (e.g., Achmus et al. 2013). In the present study, $\phi_\mu=0.65\phi'$ is used, where ϕ' (in degree)$=16D_r^2+0.17D_r+28.4$ (API, 1987).

The Young's modulus of elasticity of sand (E_s) can be expressed as a function of mean effective stress (p') as, $E_s=Kp_a\left(p'/p_a\right)^n$ (Janbu, 1963); where, K and n are soil parameters and p_a is the atmospheric pressure. However, in this study, a constant value of E_s=90 MPa is used which is a reasonable value for a dense sand having D_r=90%.

The numerical analysis is conducted in two steps. In the first step, geostatic stress is applied. In the second step, the pile is displaced in the X direction specifying a displacement boundary condition at the reference point at a vertical distance e above the pile head (Fig. 2a).

Two sets of FE analyses are performed. In the first set, analyses are performed to show the performance of the model comparing the results of FE analysis and centrifuge tests reported by Klinkvort and Hededal (2014), which is denoted as "model test simulation." In the second set a parametric study is conducted for a wide range of aspect ratio ($\eta=L/D$) of the pile and load eccentricity.

Model test simulation results

a) Simulation of Klinkvort and Hededal (2014) centrifuge test results

Four centrifuge tests (T6, T7, T8 and T9) conducted by Klinkvort and Hededal (2014) are simulated. These tests were conducted using 18 m long and 3 m diameter (prototype) monopiles installed in saturated dense sand of $D_r \approx 90\%$. The lateral load was applied at an eccentricity (e) of 27.45, 31.5, 38.25 and 45.0 m in tests T6, T7, T8 and T9, respectively.

The soil parameters used in FE simulation with the MMC model are listed in Table 2. Figure 3 shows the variation of normalized force ($H/K_p\gamma'D^3$) with normalized displacement (u/D) obtained from FE analyses along with centrifuge test results. Here, H is the lateral force, γ' is the submerged unit weight of sand, D is the diameter of the pile, K_p is the Rankine passive earth pressure coefficient calculated using API (1987) recommended ϕ' mentioned above, and u is the lateral displacement of the pile head. Note that different parameters have been used in the past to normalize H (e.g., LeBlanc et al. 2010; Achmus et al. 2013; Klinkvort and Hededal 2014); however, in order to be consistent, the vertical axis of Fig. 3 shows the normalized H as Klinkvort and Hededal (2014).

The normalized load–displacement behavior obtained from FE analyses match well with the centrifuge test results except for T7 in which FE analyses show higher initial stiffness than that reported from centrifuge test. Klinkvort and Hededal (2014) recognized this low initial stiffness in T7, although did not report the potential causes. The load–displacement curves do not become horizontal even at u/D=0.5 although the gradient of the curves at large u is small as compared to the gradient at low u. As the load–displacement curve does not reach a clear peak, a rotation criterion is used to define the ultimate capacity (H_u and M_u). Klinkvort (2012) defined the ultimate condition (failure) at θ=4° while LeBlanc et al. (2010) defined it as $\tilde{\theta} = \theta\sqrt{p_a/L\gamma'} = 4°$. In this study, defining the ultimate condition at θ=5° (i.e. $\tilde{\theta} = 3.7°$ in this case), H_u and M_u (=$H_u e$) are obtained. The rotation of the pile with vertical axis (θ) is obtained by plotting the lateral displacement of the pile with depth.

b) Effects of vertical load

The monopiles supporting offshore wind turbines also experience a vertical load due to the weight of superstructure containing the turbine and transition pieces. Typical vertical load on a 2–5 MW offshore wind turbine foundation is 2.4–10 MN (Malhotra 2011; LeBlanc et al. 2010; Achmus et al. 2013). The effects of vertical load on the lateral load-carrying capacity of monopile are examined from 21 simulations of a monopile having L=18 m and D=3 m under vertical loading V of 0, 5 and 10 MN for lateral loading at 6 different eccentricities and pure moment. The soil parameters used in the analysis are same as before (Table 2). In these simulations, after the geostatic step, the vertical load is applied gradually and then the lateral eccentric load is applied as shown in Fig. 1a.

The H_u–M_u interaction curves obtained from these 21 FE simulations for different vertical loading conditions are shown in Fig. 4a. As shown, the load-carrying capacity of a monopile increases with vertical load. In this case, H_u and M_u increase approximately by 11% for a change of V from 0 to 10 MN.

The initial stiffness (k_{in}) of the load–rotation curve is one of the main concerns in monopile design. As the H–θ curve is nonlinear, k_{in} is defined as the slope of the line drawn from origin to the point at θ=0.5° (inset of Fig. 4b). Figure 4(b) shows that k_{in} decreases with eccentricity; however, the effect of V on k_{in} is minimal. For a given eccentricity, the minimum load-carrying capacity (Fig. 4a) and stiffness (Fig. 4b) are obtained for V=0. Achmus et al. (2013) also found similar effect of V from FE simulation using the MC model. From centrifuge modeling, Alderlieste (2011) also reported decrease in stiffness with eccentricity. As the effect of V is not very significant, in the following sections, all the analyses are performed for V=0.

c) FE Simulation with Mohr-Coulomb model

The built-in Mohr-Coulomb (MC) model in Abaqus FE software is also used to simulate the response of monopiles in sand. With the MC model, the soil behavior is elastic until the stress state reaches the yield surface which is defined by the Mohr-Coulomb failure criterion. Constant values of ϕ' and ψ are needed to be given as input parameters in the MC model. As post-peak softening occurs during shearing of dense sand, estimation of appropriate values of ϕ' and ψ is a challenging task. Based on the API (1987) recommendations mentioned above ϕ'=41.5° is calculated for D_r=90%. The value of ψ (=13°) is then calculated using the relationship proposed by Bolton (1986) as $\psi=(\phi'_p-\phi'_c)/0.8$. Now using ϕ'=41.5° and ψ=13°, FE analyses are also performed using the built-in MC model. The dashed lines in Fig. 3 show the simulation results with the MC model. The MC model over-predicts the lateral load-carrying capacity together with overall high stiffness of the load–displacement curve compared to centrifuge tests and FE simulations with the MMC model.

Overestimation of the initial stiffness by the API formulation for large-diameter pile has been reported by a number of researchers (e.g., Achmus et al. 2009; Lesny et al. 2007). Alderlieste (2011) introduced a correction term to define stress-dependent soil stiffness to match the experimental load–displacement curves. Although this modification improves the prediction, it under-predicts H at low u but over-predicts at large u.

One of the main advantages of the MMC model is that the mobilized ϕ' and ψ decrease with plastic shear strain (i.e. displacement u) which reduces the shear resistance of soil and therefore the gradient of the load–displacement curves reduces with u (Fig. 3).

d) Soil failure mechanisms

The mechanisms involved in force–displacement behavior can be explained further using the formation of shear bands (plastic shear strain concentrated zones). The accumulated plastic shear strain (γ^p) in the simulation of test T9 is shown in left column of Fig. 5 for θ=0.5°, 1° and 5°. The plastic shear strains start to develop near the pile head at a small rotation (e.g., θ=0.5°) and an inclined downward shear band f_1 forms in front of the pile (right side) because of eccentric lateral loading (Fig. 5a). With the increase in θ, another inclined upward shear band f_2 forms that reaches the ground surface and creating a failure wedge as shown in Fig. 5(b). With further increase in rotation (e.g., θ=5°), the third shear band f_3 forms (Fig. 5c). During the formation of shear bands, small or negligible γ^p develops in the soil elements outside the shear bands. With increase in rotation, γ^p increases in and around the shear bands. In addition, significant plastic shear strains develop behind the pile with rotation resulting in active failure of the soil and settlement near the pile head (Fig. 5c). The right column of Fig. 5 shows the simulations using the MC model. In this case no distinct shear band is observed; instead, the zone of plastic shear strain accumulation in the right side of the pile enlarges with rotation of the pile because the post-peak softening is not considered.

The difference between the force–displacement curves obtained with the MC and MMC model could be explained further examining mobilized ϕ' and ψ along the shear bands. In the MC model, the plastic shear deformation occurs under constant ϕ' and ψ. However, in the MMC model, ϕ' and ψ varies with accumulated plastic shear strains. As shown in Fig. 5(a–c), significant accumulation of γ^p occurs in the shear bands. The mobilized ϕ' and ψ for these three values of θ (0.5°, 1° and 5°) are shown in Fig. 6. As shown in Fig. 2(b), the maximum values of ϕ' and ψ mobilize at γ^p_p, and therefore $\phi' < \phi'_p$ and $\psi < \psi_p$ in the pre-peak ($\gamma^p < \gamma^p_p$) and also in the post-peak ($\gamma^p > \gamma^p_p$) conditions. The colored zones in Figs. 5(a–c) roughly represent the post-peak condition ($\gamma^p > \gamma^p_p$) developed in soil, while in the gray zones some plastic shear strains develop ($\gamma^p < \gamma^p_p$) but the soil elements in this zone are still in the pre-peak shear zone (see Fig. 2b). The colored zones in Fig. 6 roughly represent the mobilized ϕ' (Figs. 6a–c) and ψ (Figs. 6d–f) in the post-peak while the gray areas of these figures represent the pre-peak zones. These figures show that ϕ' and ψ are not constant along the shear band rather it depends on accumulated plastic shear strain γ^p. In some segments they could be at the peak, while in the segments where large plastic shear strains accumulate ϕ' and ψ are at the critical state. As ϕ' and ψ reduce with γ^p at large strains, lower normalized lateral force is calculated with the MMC model than the MC model (Fig. 3).

It is to be noted here that FE element size influences the results when the analyses involve post-peak softening behavior of soil. A summary of regularization techniques available in the literature to reduce the effects of element size is available in Gylland (2012). Previous studies also show that a simple element size scaling rule could reduce this effect for some two-dimensional problems (Anastasopoulos et al. 2007; Dey et al. 2015; Robert 2010). The authors of the present study also recognize that an improved regularization technique for FE simulation of monopiles under lateral loading, considering the orientation of the curved shear bands and three-dimensional effects, likely involves considerable additional complexity and is left for a future study.

The parametric study presented in the following sections is conducted with the MMC model.

FE simulations for different aspect ratios

The aspect ratio η (=L/D) is often used to examine the effects of pile geometry on the load-carrying capacity. The value of η could be varied by changing the values of L or D or both. Analyses are performed for three values of η (=4, 5, 6) by varying D between 3 and 4.5 m and L between 12 and 21 m, as shown in Table 3. The lateral load is applied at 6 different eccentricities ranging between 0 and 20D. In addition, analyses are performed for pure moment condition. In other words, a total of 42 analyses for six monopiles (7 for each geometry) are conducted. The soil properties listed in Table 2 are used in the analysis.

a) Force–displacement and moment–rotation curves

The capacity of a monopile need to be estimated at different states such as the ultimate limit state (ULS) and serviceability limit state (SLS). The SLS occurs at much lower rotation of the pile than ULS. In the design, both ULS and SLS criteria need to be satisfied.

Typical force–displacement and moment–rotation curves are shown in Fig. 7(a) and 7(b), respectively, for a monopile of L=12 m and D=3 m loaded at different eccentricities. In these figures the lateral load and moment are related as M=He. Similar to Fig. 3, the load–displacement curve does not reach a clear peak and therefore the rotation criterion θ=5° is used to define the ultimate capacity. For serviceability limit state (SLS), the allowable rotation is generally less than 1° (Doherty and Gavin 2012; DNV 2011).

Figure 7(a) shows that the lateral load-carrying capacity decreases with increase in eccentricity. In this figure, the open symbols show the lateral loads for 0.5°, 1° and 5° rotations. All the points for a given rotation (e.g., open squares) are not on a vertical line in Fig. 7(a) because the depth of rotation slightly decreases with increase in eccentricity (explained later). As expected, H increases with increase in rotation (e.g., H_u for θ=5° is greater than H_u for θ=1°).

In the design of long slender piles, the lateral load at pile head displacement of 10% of its diameter is often considered as the ultimate load. The solid triangles show the lateral load-carrying capacity of the pile for 0.1D pile head displacement. In these analyses, it is higher than the lateral load at θ=1° but lower than θ=5°.

Similar to Fig. 7(a), the open symbols in Fig. 7(b) show the moments at θ=0.5°, 1° and 5°, while the solid triangles show the moment for 0.1D pile head displacement. Notice that the top most curve in Fig. 7(b) is for pure moment (not for pure lateral load as in Fig. 7(a) because in that case M=0 as e=0). Although lateral load-carrying capacity decreases with increase in eccentricity (Fig. 7a), the corresponding moment increases (Fig. 7b).

In summary, both load- and moment-carrying capacity of a large-diameter monopile in dense sand depends on its rotation. As the rotation criterion is commonly used in the current practice (DNV 2011), the values of H and M at θ=0.5°, 1° and 5° will be critically examined further in the following sections, which are denoted as $H_{0.5}$, H_1, H_5 and $M_{0.5}$, M_1, M_5, respectively. Note that, H_5 and M_5 are considered as the ultimate capacity (H_u and M_u) in this study.

b) Point of rotation

One of the limitations of the current *p–y* curve based design method is that it has been developed from test results of slender piles where only the top part of the pile deflects under lateral loading. However, a large-diameter monopile behaves similar to a rigid pile and therefore the monopile tends to rotate around a rotation point and generates pressure along the whole length of the pile.

In order to identify the point of rotation of the pile in terms of length (i.e. d/L in Fig. 1b), the lateral displacements of 3 m diameter piles of different lengths listed in Table 3 are plotted in Fig. 8. As the pile length is different (Table 3), the depth z in the vertical axis is normalized by L. Similarly, for a given θ, the lateral displacement (u) at a normalized depth (z/L) depends on the length of the pile. Therefore, for a better presentation, the lateral displacements are plotted multiplying by a length factor L_{ref}/L as $\tilde{u} = u(L_{ref}/L)$, where the 15 m long pile is considered as reference (i.e. L_{ref}=15 m). Figure 8(a) shows that the point of rotation is located approximately at d=0.78L for e=0 for all three degree of rotations. With increase in e, d/L slightly decreases (Figs. 8b and 8c). For the pure moment case, $d \approx 0.7L$ is calculated. Similar responses have been observed for other pile diameters. In summary, d/L is approximately constant irrespective of the length of the pile for a given e for these level of rotations. Moreover, $d/L \approx 0.7L$–$0.78L$ for the cases analyzed in this study. Note that, Klinkvort and Hededal (2014) also reported $d \approx 0.7L$ from a number of centrifuge model tests.

c) Force–moment interaction diagram

The capacity of a monopile can be better described using force–moment interaction diagrams (Fig. 9). In order to plot this diagram, the values of H and M are obtained for each of the 42 analyses listed in Table 3 for θ=0.5°, 1° and 5° as shown in Figs. 7(a) and 7(b). Figure 9 shows that H–M interaction lines are almost linear. The capacity (both H and M) increases with increase in length and diameter of the monopile. Comparison of Figs. 9(a)–(c) show that the capacity of the monopile increases with increase in rotation; however, the shape of the H–M curves remain almost linear for all three rotations. Similar shape of H–M diagrams have been reported by Achmus et al. (2013), where FE analyses of suction bucket foundations have been conducted using the built-in Mohr-Coulomb model with constant ϕ' and ψ.

d) Horizontal stress around the pile

The soil resistance to the lateral movement of the pile depends on two factors: (i) frontal normal stress and (ii) side friction (Briaud et al. 1983; Smith 1987). The contour plots of the horizontal compressive stresses for three different load eccentricities at $\theta=5^0$ are shown in Fig. 10 for the analysis of the monopile having $L=18$ m and $D=3$ m. Compressive stress develops in the right side of the pile up to approximately 0.70–0.78L and in the left side near the bottom of the pile. An uneven shape of the stress contour around the shear band f_3 in Fig. 5(c) is calculated (e.g., see the stress contour around the line AB in Fig. 10a). The pattern is similar for all three eccentricities. The solid circles show the approximate location of the point of rotation.

d) Effects of η and e on initial stiffness

Similar to Fig. 4(b), the initial stiffness (k_{in}) is calculated for all 42 analyses listed in Table 3 and plotted in Fig. 11. The initial stiffness increases with increase in size of the pile and the increase is very significant at low eccentricities; however, at large e/D, the difference in k_{in} is relatively small. For a given pile length (e.g., $L=18$ m), k_{in} is higher for larger diameter pile up to $e=5D$; however, k_{in} is almost independent of D at large eccentricities (e.g., $e=15D$). This is consistent with centrifuge tests (Alderlieste 2011) where it was shown that the decrease in stiffness with eccentricity is more pronounced in larger diameter piles. Similar findings have been reported by Achmus et al. (2013) for suction bucket foundations.

Proposed equation for lateral load-carrying capacity and moment

Various theoretical methods have been proposed in the past to calculate the ultimate lateral resistance (H_u) of free-headed laterally loaded rigid pile based on simplified soil pressure distribution along the length of the pile (Brinch Hansen 1961; Broms 1964; Petrasovits and Award 1972; Meyerhof et al. 1981; Prasad and Chari 1999). Following LeBlanc et al. (2010), an idealized horizontal pressure distribution (p) shown in Fig. 1(b) is used to estimate the lateral load-carrying capacity. Note that the assumed shape of p in Fig. 1(b) is similar to the horizontal pressure distribution obtained from FE analysis (Fig. 10). From Fig. 1(b), the force and moment equilibrium equations at the pile head can be written as:

$$H = \frac{1}{2}KD\gamma'(2d^2 - L^2) \quad (1)$$

$$M = \frac{1}{3}KD\gamma'(L^3 - 2d^3) \quad (2)$$

Combining Eqs. (1) and (2), and replacing $M=He$, the following relationship is obtained:

$$4R^3 + 6R^2\frac{e}{L} - \left(2 + 3\frac{e}{L}\right) = 0 \qquad \text{where, } R=d/L \quad (3)$$

For a given e/L, Eq. (3) is solved for R which is then used to find d. Now inserting d in Eq. (1) and (2), H and M are calculated.

In addition to the shape of the pressure distribution profile (Fig. 1b), the estimation of parameter K is equally important. Broms (1964) assumed $K=3K_p$ (i.e. $p=3K_pD\gamma'z$) for the entire length in front of the pile to calculate H_u. Comparison of field test results show that Broms' method underestimates H_u (Poulos and Davis 1980), especially for piles in dense sand (Barton 1982). Therefore, Barton (1982) suggested $K=K_p^2$.

A close examination of all the FE results presented above show that the H_u calculated using Eqs. (1)–(3) reasonably match the FE results at $\theta=5^0$ if $K=4.3K_p$ is used. The open squares in Fig. 12 show that the calculated H_u using the empirical Eqs. (1)–(3) match well with the FE results. In this figure, H is plotted in normalized form as $\overline{H} = H / K_p \gamma' D L^2$. As shown before that the lateral load-carrying capacity increases with decreasing eccentricity (Fig. 7a). Therefore, for a given rotation, the points with higher $\overline{H}_u$ represent the results for lower eccentricities. The rightmost points, where the maximum discrepancy is found, are for the purely lateral load applied to the pile head (e=0). The discrepancy is not very significant for high eccentricities. As in offshore monopile foundations the lateral load acts at relatively high eccentricity, Eqs. (1)–(3) and FE results show better match for these loading conditions.

In order to provide a simplified guideline for SLS design, capacities of the monopile at two more rotations (θ=0.5° and 1°) are also investigated. Reanalyzing H at these rotations, it is found that if K=1.45K_p and 2.25K_p are used for θ=0.5° and 1°, respectively, the calculated H using Eqs. (1)–(3) reasonably match the FE results (Fig. 12). Similar to the mobilization of the passive resistance behind a retaining wall with its rotation, this can be viewed as: at θ equals 0.5° and 1°, respectively, the mobilized K is 34% and 52% of the K at the ultimate condition (θ=5°).

Lateral force–moment interaction

Figure 13 shows the lateral force–moment interaction diagram in which H and M are normalized as $\overline{H} = H / K_p \gamma' D L^2$ and $\overline{M} = M / K_p \gamma' D L^3$. The solid lines are drawn using Eqs. (1)–(3) for θ=0.5°, 1° and 5° using K=1.45K_p, 2.25K_p and 4.3K_p, respectively, as described before. The scattered points (open triangles, squares and circles) show the values obtained from FE analysis for these three levels of rotation. Purely a lateral load at the pile head as shown in the vertical axis or purely a moment without any H as shown in the horizontal axis are not expected in offshore monopile foundations for wind turbine because H acts at an eccentricity. However, these analyses are conducted for the completeness of the interaction diagram. As shown in this figure, with increase in eccentricity (i.e. $\overline{M}$) the lateral load-carrying capacity $\overline{H}$ decreases. The calculations using the simplified equations with the recommended values of K reasonably match the FE results for these three levels of rotation. The shape of the $\overline{M}-\overline{H}$ interaction diagram is similar to experimental observation (LeBlanc et al. 2010) and numerical modeling of large-diameter suction bucket foundation (Achmus et al. 2013).

Reanalyzing available model test results, Zhang et al. (2005) proposed an empirical method to calculate the ultimate lateral load-carrying capacity of rigid pile considering both soil pressure and pile–soil interface resistance. They calculated the depth of rotation using the empirical equation proposed by Prasad and Chari (1999). Calculated H_u and M_u (=$H_u e$) using this empirical method (Zhang et al. 2005) for the eccentricities considered in the present FE analysis are also shown in Fig. 13. The ultimate capacity of the large-diameter monopiles (at θ=5°) is approximately 35% higher than the Zhang et al. (2005) empirical model.

As M=He, the slope of a line drawn from the origin in the $\overline{M}-\overline{H}$ plot (Fig. 13) is L/e. In order to explain this diagram and to provide a worked example, consider a monopile of D=4 m and L=18 m installed in dense sand of D_r=80% and γ'=10 kN/m^3, and is subjected to an eccentric lateral load acting at e=50 m above the pile head. For this geometry, draw the line OA at a slope of L/e=0.36 (Fig. 13). From the intersections of this line with $\overline{M}-\overline{H}$ interaction diagram (solid lines), the normalized capacity of the pile $\overline{H}$ can be calculated as 0.04, 0.06, 0.12 for θ=0.5°, 1° and 5°, respectively. Now calculating ϕ'=38.8° based on API (1987), K_p=4.36 can be obtained, which gives lateral load-carrying capacities of 2.26, 3.39, 6.78 MN and corresponding moments of 113, 170 and 339 MN-m for θ=0.5°, 1° and 5°, respectively.

Conclusions

Three-dimensional FE analyses are performed to estimate the lateral load-carrying capacity of monopiles in dense sand for different load eccentricities. Analyses are mainly conducted by employing a modified form of Mohr-Coulomb model (MMC) that captures the typical stress–strain behavior of dense sand. The following conclusions can be drawn from this study.

1. FE analysis with the MMC model simulates the load–displacement behavior for a wide range of lateral displacement of the pile head, including the reduction of stiffness at large displacements, as observed in centrifuge model tests.
2. With the MMC model the mobilization of ϕ' and ψ with rotation of the pile creates distinct shear bands due to post-peak softening, which could not be simulated using the Mohr-Coulomb model.
3. The load-carrying capacity of the pile depends on its rotation. For 0.5° and 1° rotation of the pile the mobilized capacity is approximately 34% and 52%, respectively, of the ultimate capacity calculated at 5° rotation.
4. At the ultimate loading condition the depth of the point of rotation of the pile is approximately $0.7L$ for monopiles used in offshore wind turbine foundation loaded at large eccentricity.
5. The simplified model based on a linear pressure distribution, with a pressure reversal at the point of rotation, can be used for preliminary estimation of load-carrying capacity. The normalized capacity of large-diameter monopiles is higher than the estimated capacity of small-diameter piles based on the empirical equations developed from small-scale model test results.

Finally, it is to be noted that the effects of long-term cyclic loading on monopiles is another important issue which has not been investigated in the present study.

Acknowledgements

The work presented in this paper has been funded by NSERC Discovery grant, MITACS and Petroleum Research Newfoundland and Labrador (PRNL).

References

ABAQUS. (2013). Abaqus User's Manual. Version 6.13-1, Dassault Systèmes.

Abdel-Rahman, K., and Achmus, M. (2005). "Finite element modelling of horizontally loaded monopile foundations for offshore wind energy converters in Germany." *Proc., International Symposium on Frontiers in Offshore Geotechnics*, Perth, Australia, 6p.

Abdel-Rahman, K., and Achmus, M. (2006). "Behaviour of monopile and suction bucket foundation systems for offshore wind energy plants." *Proc., 5th International Engineering Conference*, Sharm El-Sheikh, Egypt, 9p.

Achmus, M., Akdag, C.T., and Thieken, K. (2013). "Load-bearing behavior of suction bucket foundations in sand." *Applied Ocean Research*, 43, 157–165.

Achmus, M., Kuo, Y.S., and Abdel-Rahman, K. (2009). "Behavior of monopile foundations under cyclic lateral load." *Computers and Geotechnics*, 36, 725–735.

Achmus, M., and Thieken, K. (2010). "On the behavior of piles in non-cohesive soil under combined horizontal and vertical loading." *Acta Geotechnica*, 5(3), 199–210.

Alderlieste, E. A. (2011). "Experimental modelling of lateral loads on large diameter monopile foundations in sand." M.Sc. thesis, Delft University of Technology, 120p.

Anastasopoulos, I., Gazetas, G., Bransby, M. F., Davies, M. C. R. and Nahas, A. El. (2007). "Fault rupture propagation through sand: finite-element analysis and validation through centrifuge experiments." *J. of the Geotech. and Geoenviron. Eng.*, ASCE, 133(8), 943–958.

API. (1987). “Recommended practice for planning, designing and constructing fixed offshore platforms.” API Recommended practice 2A (RP 2A). 17th ed., American Petroleum Institute.

API. (2011). ANSI/API recommended practice, 2GEO 1st ed., Part 4, American Petroleum Institute.

Barton, Y. O. (1982). “Laterally loaded model piles in sand: centrifuge tests and finite element analyses,” PhD thesis, University of Cambridge.

Bolton, M. D. (1986). “The strength and dilatancy of sand.” *Géotechnique*, 36(1), 65–78.

Briaud, J.-L., Smith, T. D., and Meyer, B. J. (1983). “Using the pressuremeter curve to design laterally loaded piles.” *Proc., 15th Offshore Technology Conf.*, Houston, Paper #4501, 495–502.

Brinch Hansen, J. (1961). “The ultimate resistance of rigid piles against transversal forces.” *Bulletin No. 12*, Danish Geotechnical Institute, Copenhagen, Denmark, 5–9.

Broms, B. B. (1964). “Lateral resistance of piles in cohesive soils.” J. *Soil Mech. Found. Div.*, ASCE, 90(2), 27–64.

Budhu, M., and Davies, T. (1987). “Nonlinear analysis of laterally loaded piles in cohesionless soils.” *Can. Geotech. J.*, 24(2), 289–296.

Carter, J. P., and Kulhawy, F. H. (1988). “Analysis and design of drilled shaft foundations socketed into rock.” Electric Power Research Institute, EPRI EL-5918, Project 1493-4.

CFEM. (2006). Canadian foundation engineering manual. 4th ed., Canadian Geotechnical Society, Richmond, BC, Canada. 506p.

Chakraborty, T., and Salgado, R. (2010). “Dilatancy and shear strength of sand at low confining pressures.” *Journal of Geotechnical and Geoenvironmental Engineering*, 136(3), 527–532.

Coduto, D. P. (2001). Foundation design: principles and practices, 2nd ed., Prentice Hall, Upper Saddle River, New Jersey, United States. 883p.

Cuéllar, V. P. (2011). “Pile foundations for offshore wind turbines: numerical and experimental investigations on the behaviour under short-term and long-term cyclic loading.” Dr.-Ing. thesis, Technical University of Berlin. 273p.

DNV. (2011). “Design of offshore wind turbine structures.” Offshore Standard, DNV-OS-J101, Det Norske Veritas. 213p.

Dey, R., Hawlader, B., Phillips, R., Soga, K. (2015). “Large deformation finite element modeling of progressive failure leading to spread in sensitive clay slopes.” *Géotechnique*, 65(8):657 – 668.

Dobry, R., Vincente, E., O’Rourke, M., and Roesset, J. (1982). “Stiffness and damping of single piles.” *J. Geotech. Engrg. Div.*, ASCE, 108 (3), 439–459.

Doherty, P., Li, W., Gavin, K., and Casey, B. (2012). “Field lateral load test on monopile in dense sand.” *Offshore Site Investigation and Geotechnics: Integrated Technologies-Present and Future*, 12–14 September, London, UK.

Doherty, P., and Gavin, K. (2012). “Laterally loaded monopile design for offshore wind farms.” *Proc., ICE-Energy*, 165(1), 7–17.

Ebin, D. M. A. (2012). “The response of monopile wind turbine foundations in sand to cyclic loading.” M.Sc. thesis, Tufts University. 112p.

Gylland AS. (2012). “Material and slope failure in sensitive clays.” PhD thesis, Norwegian University of Science and Technology.

Hearn, E. N., and Edgers, L. (2010). “Finite element analysis of an offshore wind turbine monopile.” *GeoFlorida: Advances in Analysis, Modeling & Design*, 1857–1865.

Houlsby, G. T. (1991). “How the dilatancy of soils affects their behavior.” *Proc., 10th Eur. Conf. in Soil Mech. and Found. Engrg.*, 1189–1202.

Hsu, S. T. (2005). “A constitutive model for the uplift behavior of anchors in cohesionless soils.” *Journal of the Chinese Institute of Engineers*, 28(2), 305–317.

Hsu, S. T., and Liao, H. J. (1998). “Uplift behaviour of cylindrical anchors in sand.” *Canadian Geotechnical Journal*, 34, 70–80.

Ibsen, L., Larsen, K., and Barari, A. (2014). “Calibration of failure criteria for bucket foundations on drained sand under general loading.” *Journal of Geotechnical and Geoenvironmental Engineering*, 140(7): 04014033, 16 p.

Janbu, N. (1963). “Soil compressibility as determined by oedometer and triaxial test.” *Proc., 3rd European Conference on Soil Mechanics and Foundation Engineering*. Wiesbaden, Germany, 1, 19–25.

Klinkvort, R. T. (2012). “Centrifuge modelling of drained lateral pile-soil response: application for offshore wind turbine support structures.” PhD thesis, Technical University of Denmark. 232p.

Klinkvort, R. T., and Hededal, O. (2011). “Centrifuge modelling of offshore monopile foundation.” *Frontiers in Offshore Geotechnics II*, ed. 1, Taylor & Francis, 581–586.

Klinkvort, R. T., and Hededal, O. (2014). “Effect of load eccentricity and stress level on monopile support for offshore wind turbines.” *Canadian Geotechnical Journal*, 51(9), 966–974.

Klinkvort, R. T., Leth C. T., and Hededal, O. (2010). “Centrifuge modelling of a laterally cyclic loaded pile.” *Physical Modelling in Geotechnics (Springman, S, Laue, J and Seward, L (eds.))*, CRC Press, London, UK, 959–964.

Kuo, Y. S., Achmus, M., and Abdel-Rahman, K. (2011). "Minimum embedded length of cyclic horizontally loaded monopiles." *Journal of Geotechnical and Geoenvironmental Engineering*, 138(3), 357–363.

LeBlanc, C., Houlsby, G. T., and Byrne, B. W. (2010). "Response of stiff piles in sand to long-term cyclic lateral loading." *Géotechnique*, 60(2), 79–90.

Lee, J. H., Salgado, R., and Paik, K. H. (2003). "Estimation of load capacity of pipe piles in sand based on cone penetration test results." *Journal of Geotechnical and Geoenvironmental Engineering*, 129(6), 391–403.

Lesny, K., and Wiemann, J. (2006). "Finite-element-modelling of large diameter monopiles for offshore wind energy converters." *Proc., GeoCongress 2006: Geotechnical Engineering in the Information Technology Age*, 1–6.

Lesny, K., Paikowsky, S. G., and Gurbuz, A. (2007). "Scale effects in lateral load response of large diameter monopiles," *Proc., Sessions of Geo-Denver*, Denver, Colorado, USA, Geotechnical Special Publication no. 158, 10 p.

Lings, M. L., and Dietz, M. S. (2004) "An improved direct shear apparatus for sand." *Géotechnique*, 54(4), 245–256.

Malhotra, S. (2011). "Selection, design and construction of offshore wind turbine foundations." *Wind Turbines*, Dr. Ibrahim Al-Bahadly (Ed.), ISBN: 978-953-307-221-0, InTech, 652p.

Meyerhof, G. G., Mathur, S. K., and Valsangkar, A. J. (1981). "Lateral resistance and deflection of rigid wall and piles in layered soils." *Can. Geotech. J.*, 18, 159–170.

Møller, I. F., and Christiansen, T. H. (2011). "Laterally loaded monopile in dry and saturated sand-static and cyclic loading: experimental and numerical studies." Masters project, Aalborg University Esbjerg. 93p.

Petrasovits, G., and Award, A. (1972). "Ultimate lateral resistance of a rigid pile in cohesionless soil." *Proc., 5th European Conf. on SMFE*, Madrid, 3, 407–412.

Potyondy, J. G. (1961). "Skin friction between various soils and construction materials." *Géotechnique*, 11(4), 339–353.

Poulos, H. G., and Davis, E. H. (1980). "Pile foundation analysis and design," John Wiley & Sons, New York, NY. 397p.

Poulos, H. G., and Hull, T. (1989). "The role of analytical geomechanics in foundation engineering." *Foundation engineering: Current principles and practices*, ASCE, Reston, 2, 1578–1606.

Prasad, V. S. N. Y., and Chari, T. R. (1999). "Lateral capacity of model rigid piles in cohesionless soils." *Soils and Foundations*, 39(2), 21–29.

Reese, L. C., Cox, W. R., and Koop, F. D. (1974). "Analysis of laterally loaded piles in sand." *Offshore Technology Conference*, Houston, Texas, USA, OTC 2080, 11p.

Robert, D. J. (2010). "Soil-pipeline interaction in unsaturated soils." PhD thesis, University of Cambridge, United Kingdom.

Roy, K. S., Hawlader B. C., and Kenny, S. (2014). "Influence of low confining pressure on lateral soil/pipeline interaction in dense sand." *Proc., 33rd International Conference on Ocean, Offshore and Arctic Engineering (OMAE2014)*, San Francisco, California, USA, June 8–13, 9p.

Roy, K. S., Hawlader, B. C., Kenny, S., and Moore, I. (2015). "Finite element modeling of lateral pipeline–soil interactions in dense sand." *Canadian Geotechnical Journal*, 10.1139/cgj-2015-0171.

Schanz, T., and Vermeer, P. A. (1996). "Angles of friction and dilatancy of sand." *Géotechnique*, 46(1), 145–151.

Smith, T. D. (1987). “Pile horizontal soil modulus values.” *Journal of Geotechnical Engineering*, 113(9), 1040–1044.

Sørensen, S. P. H., Brødbæk, K. T., Møller, M., Augustesen, A. H., and Ibsen. L. B. (2009). “Evaluation of the load-displacement relationships for large-diameter piles in sand.” *Proc., 12th International Conference on Civil, Structural and Environmental Engineering Computing*, Paper 244, 19p.

Tatsuoka, F., Sakamoto, M., Kawamura, T., and Fukushima, S. (1986). "Strength and deformation characteristics of sand in plane strain compression at extremely low pressures.” *Soils and Foundations*, 26(1), 65–84.

Tatsuoka, F., Siddiquee, M. S. A., Park, C. S., Sakamoto, M., and Abe, F. (1993), “Modeling stress–strain relations of sand,” *Soils and Foundations*, 33(2), 60–81.

Tiwari, B., Ajmera, B., and Kaya, G. (2010). “Shear strength reduction at soil–structure interaction.” *GeoFlorida 2010: Advances in Analysis, Modeling & Design*, Orlando, Florida, United States, February 20–24, 1747–1756.

Tiwari, B., and Al-Adhadh, A. R. (2014). “Influence of relative density on static soil–structure frictional resistance of dry and saturated sand.” *Geotechnical and Geological Engineering*, 32, 411–427.

Vermeer, P. A., and deBorst, R. (1984). “Non-associated plasticity for soils, concrete, and rock.” *Heron*, 29(3), 5–64.

Wolf, T. K., Rasmussen, K. L., Hansen, M., Ibsen, L. B., and Roesen, H. R. (2013). “Assessment of *p*–*y* curves from numerical methods for a non-slender monopile in cohesionless soil.” Aalborg: Department of Civil Engineering, Aalborg University, DCE Technical Memorandum, no. 24. 10p.

Zhang, L., Silva, F., and Grismala, R. (2005). “Ultimate lateral resistance to piles in cohesionless soils.” *Journal of Geotechnical and Geoenvironmental Engineering*, 131(1), 78–83.

Table 1. Equations for Modified Mohr-Coulomb Model (MMC) (summarized from Roy et al., 2014, 2015)

Description	Constitutive Equation
Relative density index	$I_R = I_D(Q - \ln p') - R$, where $I_D = D_r(\%)/100$, $Q = 7.4 + 0.6\ln(\sigma'_c)$ (Chakraborty and Salgado, 2010) and $R = 1$ (Bolton, 1986)
Peak friction angle	$\phi'_p - \phi'_c = A_\psi I_R$
Peak dilation angle	$\psi_p = \dfrac{\phi'_p - \phi'_c}{k_\psi}$
Strain softening parameter	$\gamma^p_c = C_1 + C_2 I_D$
Plastic strain at ϕ'_p	$\gamma^p_p = \gamma^p_c \left(p'/p'_a\right)^m$
Mobilized friction angle at Zone-II	$\phi' = \phi'_{in} + \sin^{-1}\left[\left(\dfrac{2\sqrt{\gamma^p \times \gamma^p_p}}{\gamma^p + \gamma^p_p}\right)\sin\left(\phi'_p - \phi'_{in}\right)\right]$
Mobilized dilation angle at Zone-II	$\psi = \sin^{-1}\left[\left(\dfrac{2\sqrt{\gamma^p \times \gamma^p_p}}{\gamma^p + \gamma^p_p}\right)\sin\left(\psi_p\right)\right]$
Mobilized friction angle at Zone-III	$\phi' = \phi'_c + \left(\phi'_p - \phi'_c\right)\exp\left[-\left(\dfrac{\gamma^p - \gamma^p_p}{\gamma^p_c}\right)^2\right]$
Mobilized dilation angle at Zone-III	$\psi = \psi_p \exp\left[-\left(\dfrac{\gamma^p - \gamma^p_p}{\gamma^p_c}\right)^2\right]$
Notes: A_ψ: slope of ($\phi'_p - \phi'_c$) vs. I_R; m, C_1, C_2: soil parameters; I_R: relative density index; k_ψ: slope of ($\phi'_p - \phi'_c$) vs. ψ_p; ϕ'_{in}: ϕ' at the start of plastic deformation; ϕ'_p: peak friction angle; ϕ'_c: critical state friction angle; ψ_p: peak dilation angle; ψ_{in}: ψ at the start of plastic deformation (=0); γ^p: plastic shear strain; γ^p_p: γ^p required to mobilize ϕ'_p; γ^p_c: strain softening parameter. Figure 2(b) shows the typical variation of ϕ' and ψ.	

Table 2. Soil parameters used in FE analyses

Parameters	Value
ν_{soil}	0.3
A_ψ	3.8
k_ψ	0.6
ϕ'_{in}	29°
C_1	0.22
C_2	0.11
m	0.25
Critical state friction angle, ϕ'_c	31°
Young's modulus, E_s (MN/m^2)	90
Relative density, D_r (%)	90
Submerged unit weight, γ' (kN/m^3)	10.2
Interface friction coefficient, μ	tan (0.65ϕ')
Cohesion (c')[1] (kN/m^2)	0.10

[1]Cohesion is required to be defined in Abaqus FE analysis. For sand in this study a very small value of c'=0.10 kN/m^2 is used.

Table 3 Dimensions of pile for parametric study

Aspect ratio, η=*L*/*D*			Load eccentricity, *e*
η=4	η=5	η=6	
L=12 m, *D*=3 m *L*=18 m, *D*=4.5 m	*L*=15 m, *D*=3 m *L*=18 m, *D*=3.6 m	*L*=18 m, *D*=3 m *L*=21 m, *D*=3.5 m	0, 2.5*D*, 5*D*, 10*D*, 15*D*, 20*D* and pure moment

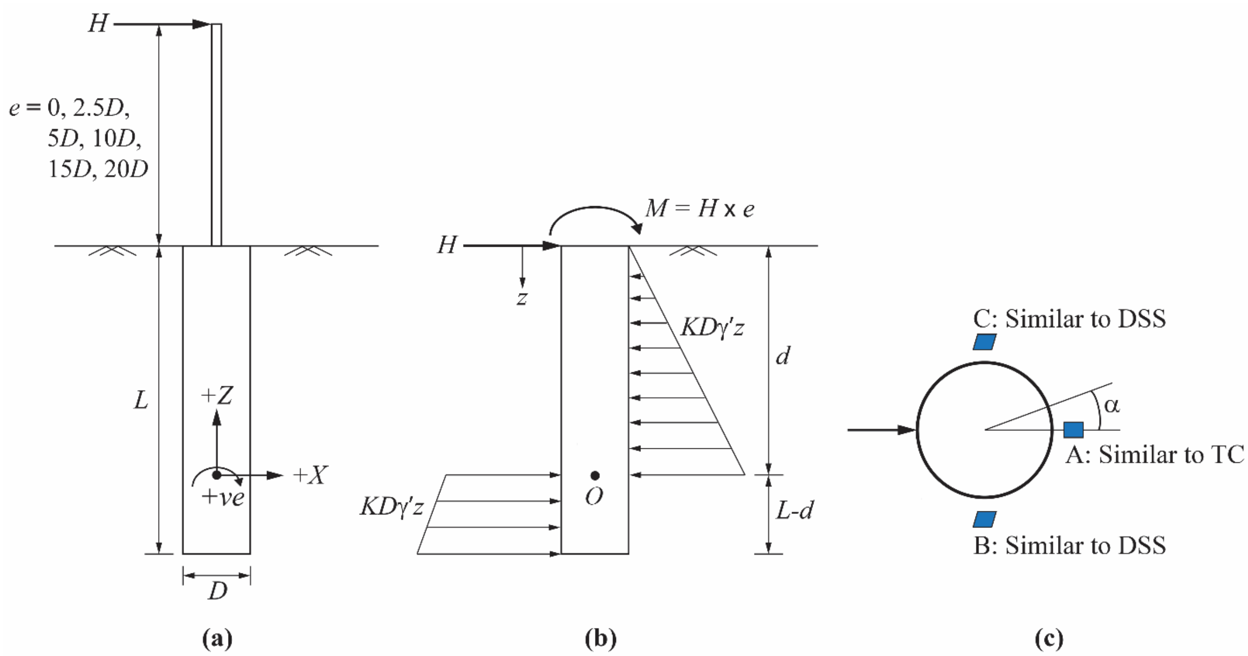

Fig. 1. Problem statement: (a) loading and sign convention, (b) assumed pressure distribution, (c) mode of shearing of soil elements

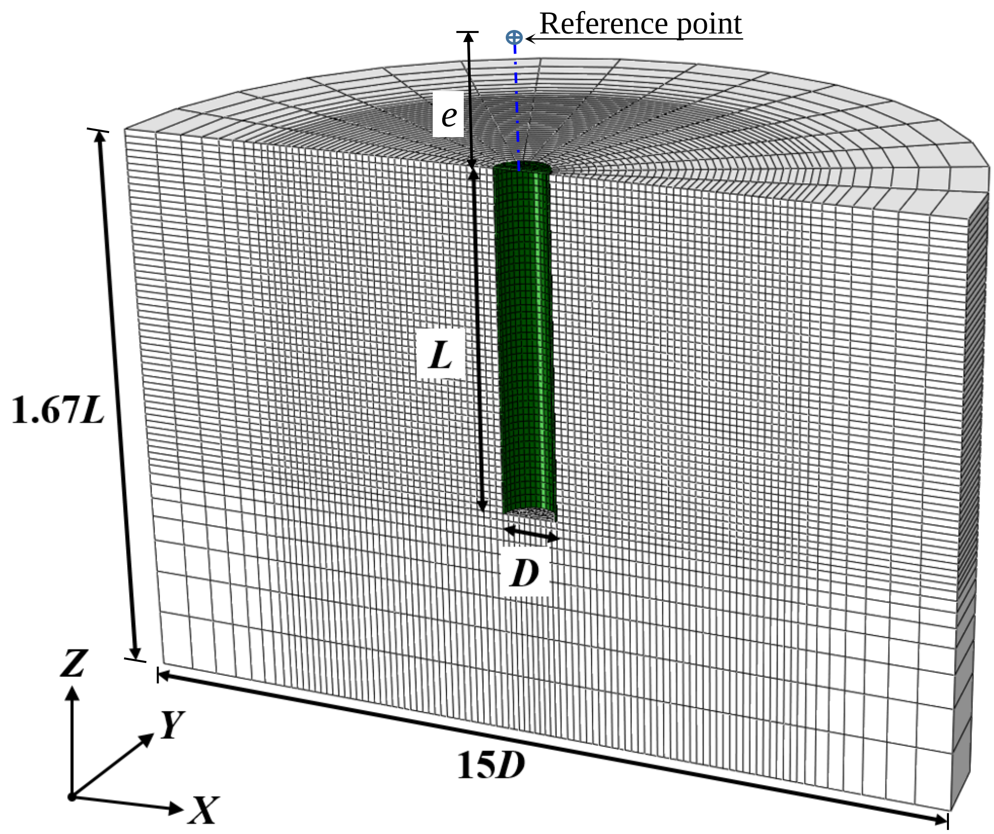

Fig. 2(a). FE mesh used in this study

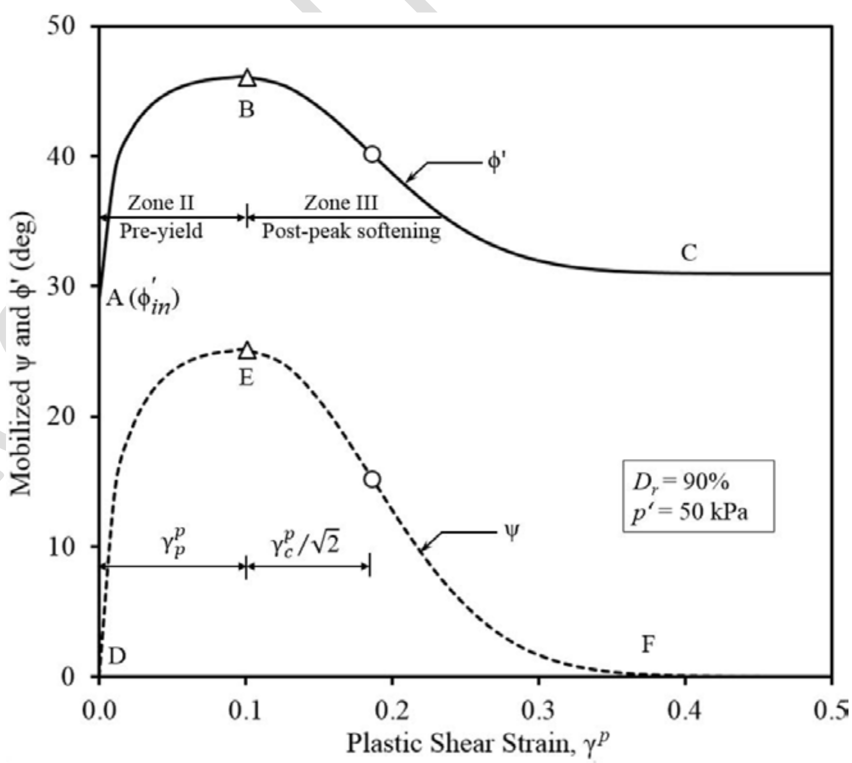

Fig. 2(b). Variation of mobilized friction and dilation angle

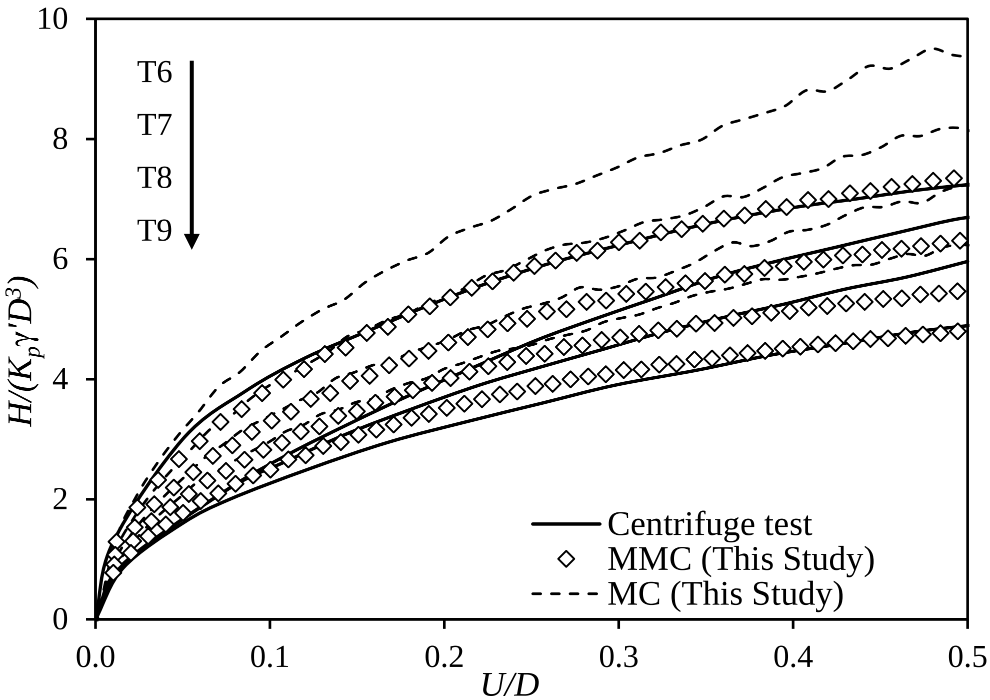

Fig. 3. Comparison between FE simulation and centrifuge test results by Klinkvort and Hededal (2014)

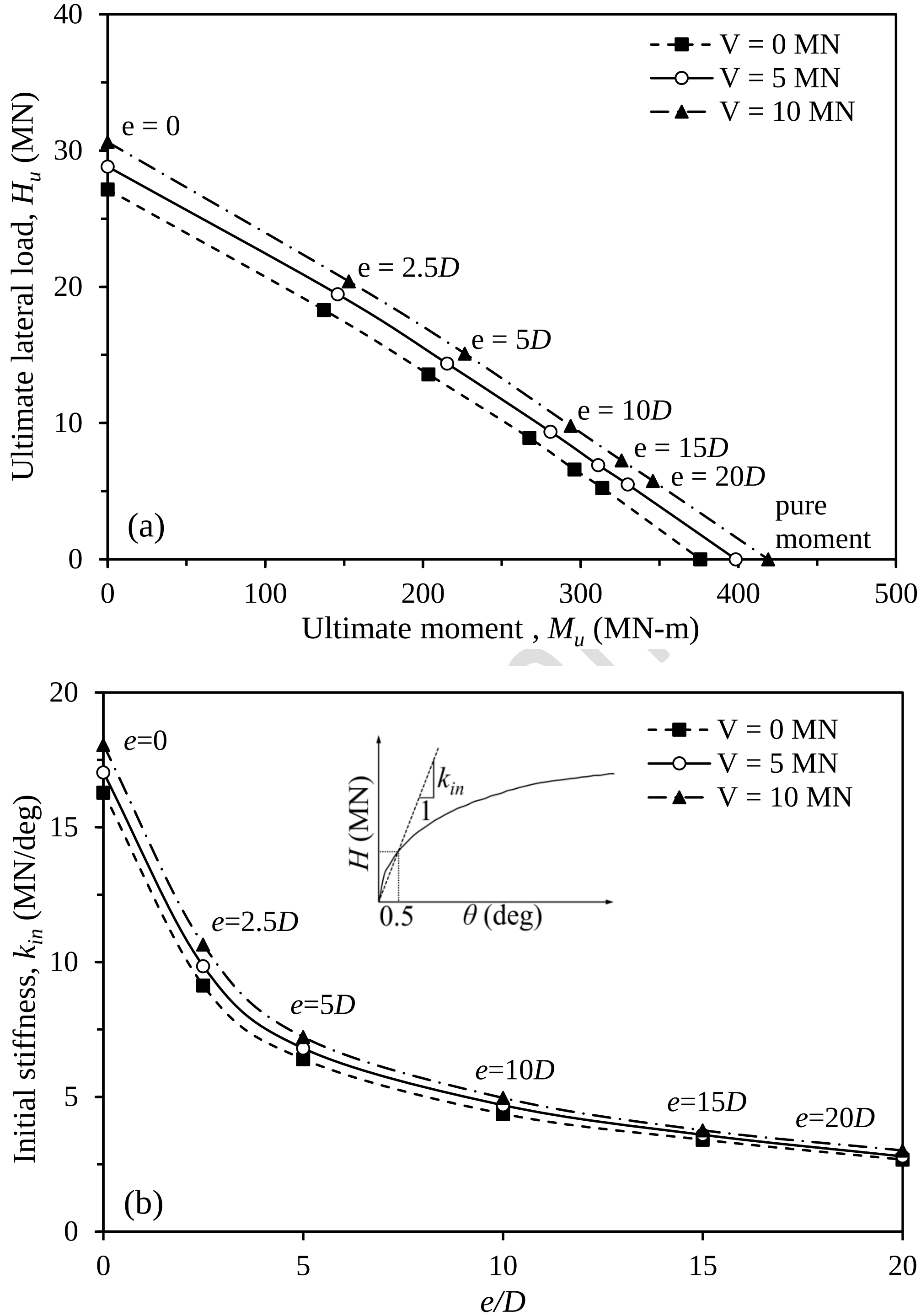

Fig. 4. Effects of vertical load and eccentricity on ultimate capacity and initial stiffness

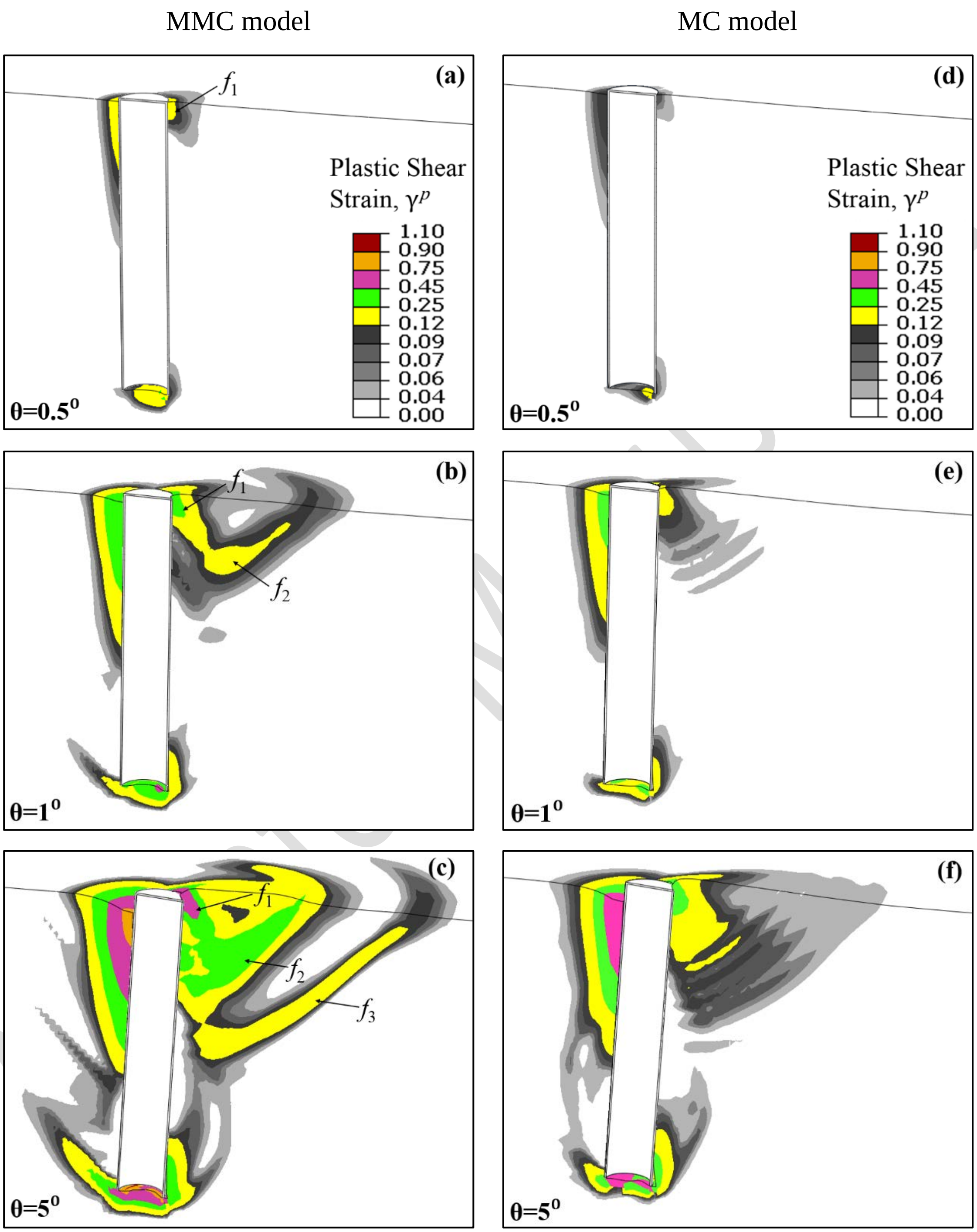

Fig. 5. Development of plastic shear zone around the monopile

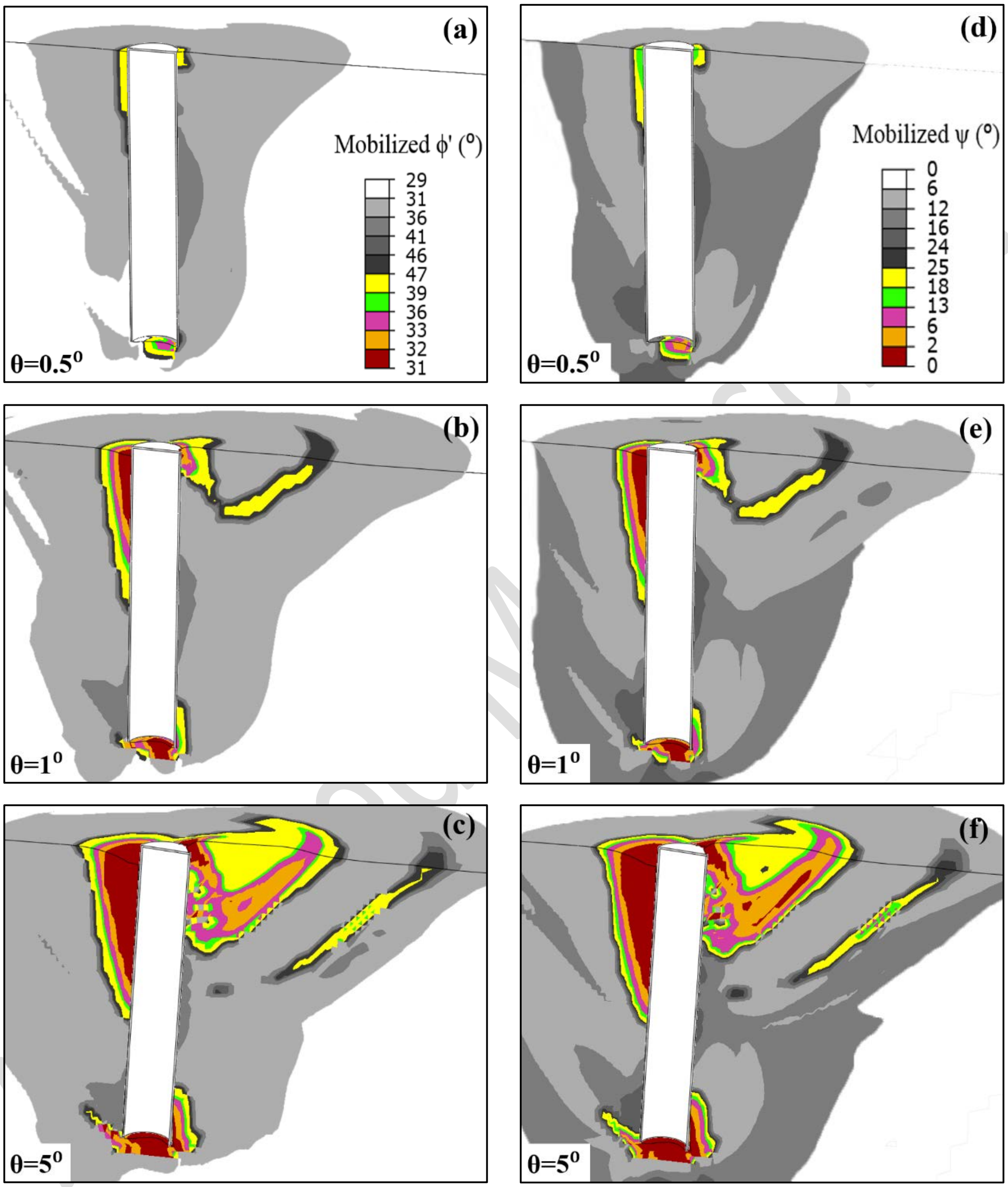

Fig. 6. Mobilized ϕ' and ψ around the monopile

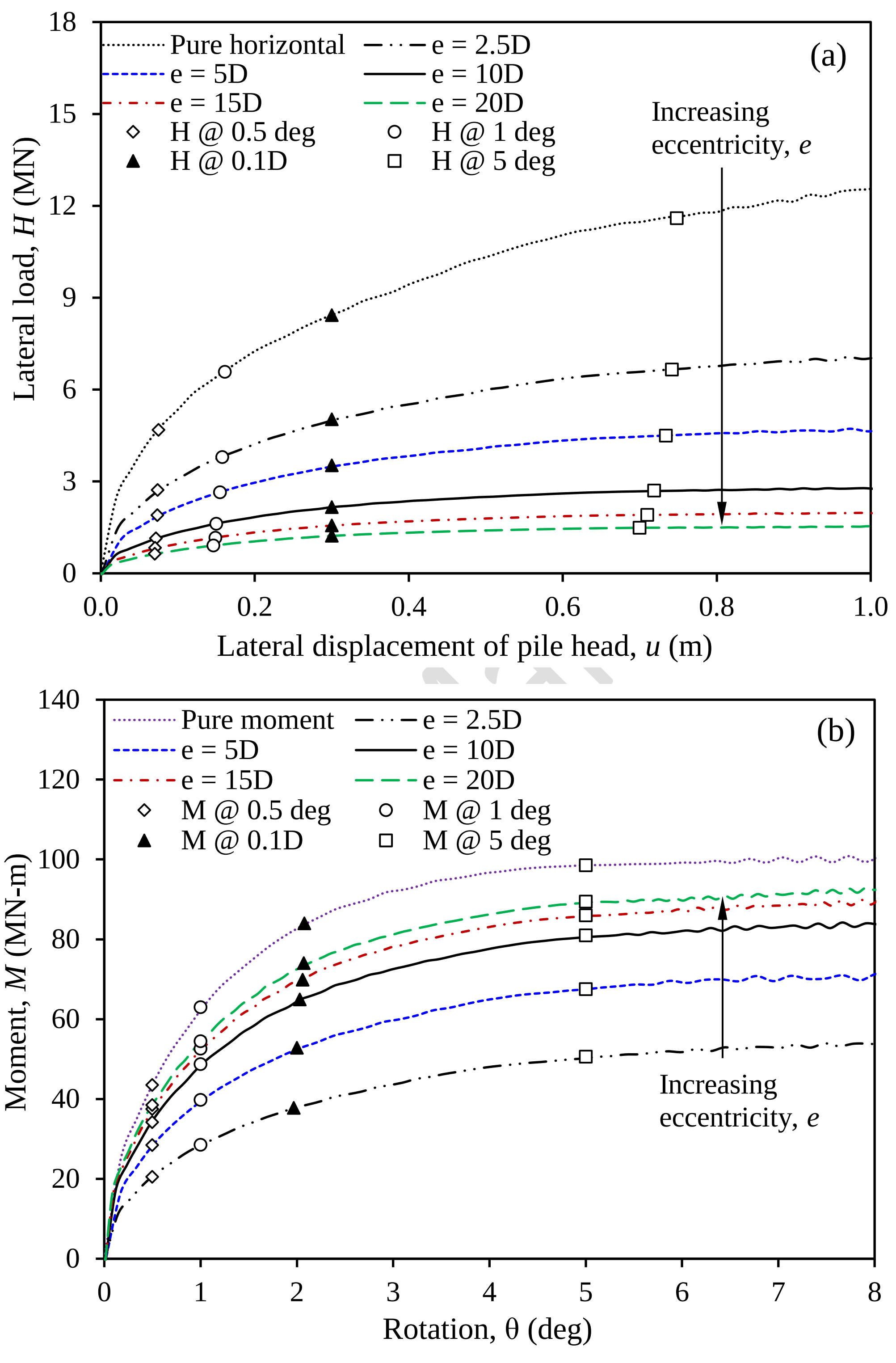

Fig. 7. Analysis for L=12 m and D=3 m: (a) lateral force–displacement, (b) moment–rotation curves

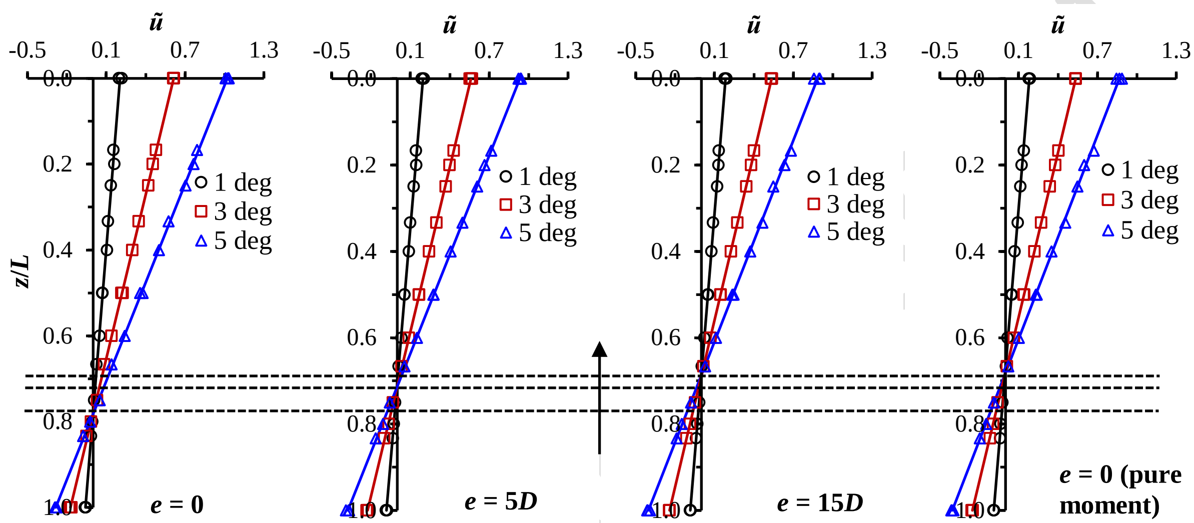

Fig. 8. Lateral displacement for different length-to-diameter ratios and eccentricities

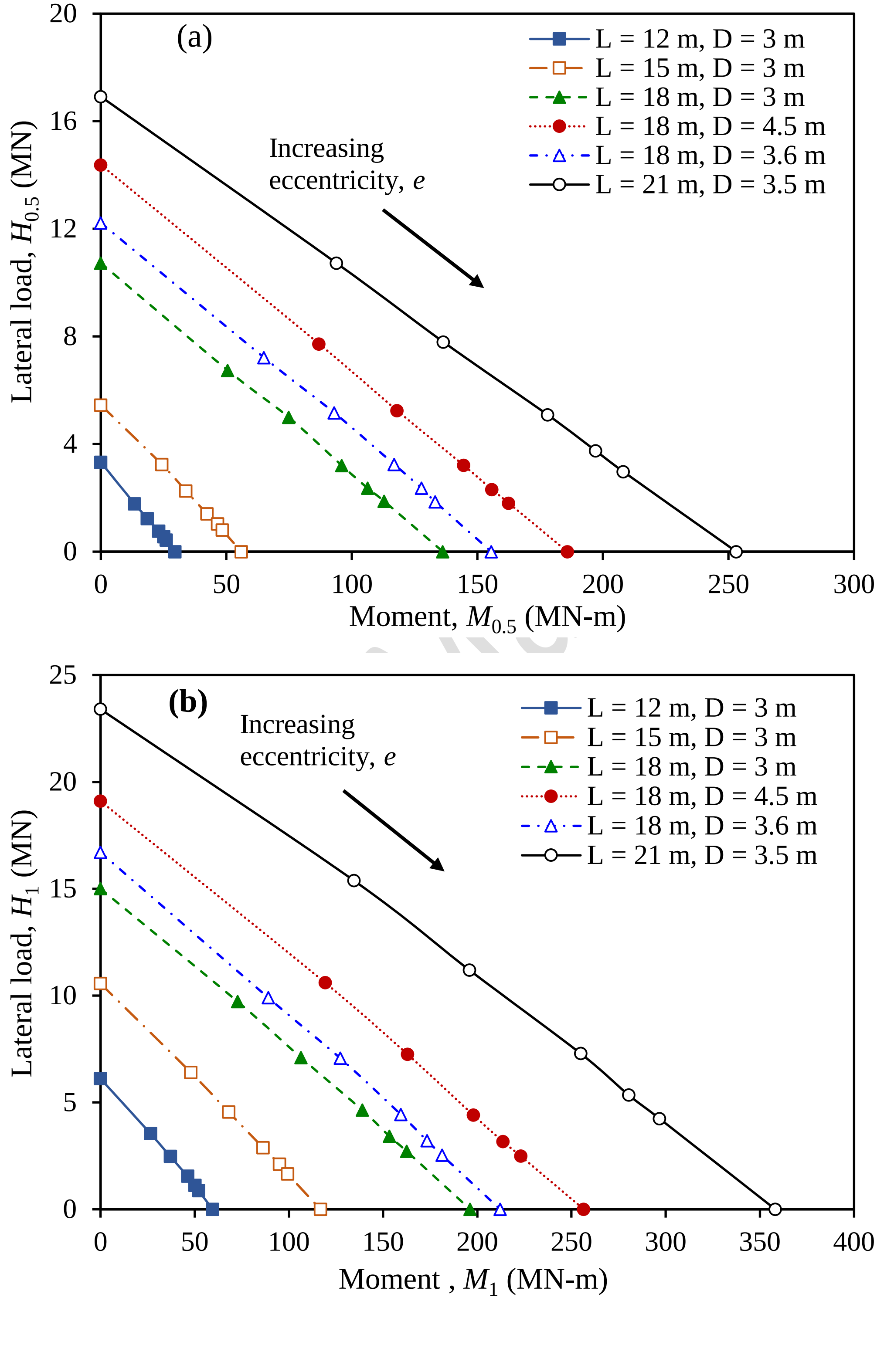

(a)
L = 12 m, D = 3 m
L = 15 m, D = 3 m
L = 18 m, D = 3 m
L = 18 m, D = 4.5 m
L = 18 m, D = 3.6 m
L = 21 m, D = 3.5 m
Increasing eccentricity, e
Lateral load, H0.5 (MN)
Moment, M0.5 (MN-m)
0
4
8
12
16
20
0
50
100
150
200
250
300
(b)
L = 12 m, D = 3 m
L = 15 m, D = 3 m
L = 18 m, D = 3 m
L = 18 m, D = 4.5 m
L = 18 m, D = 3.6 m
L = 21 m, D = 3.5 m
Increasing eccentricity, e
Lateral load, H1 (MN)
Moment , M1 (MN-m)
0
5
10
15
20
25
0
50
100
150
200
250
300
350
400

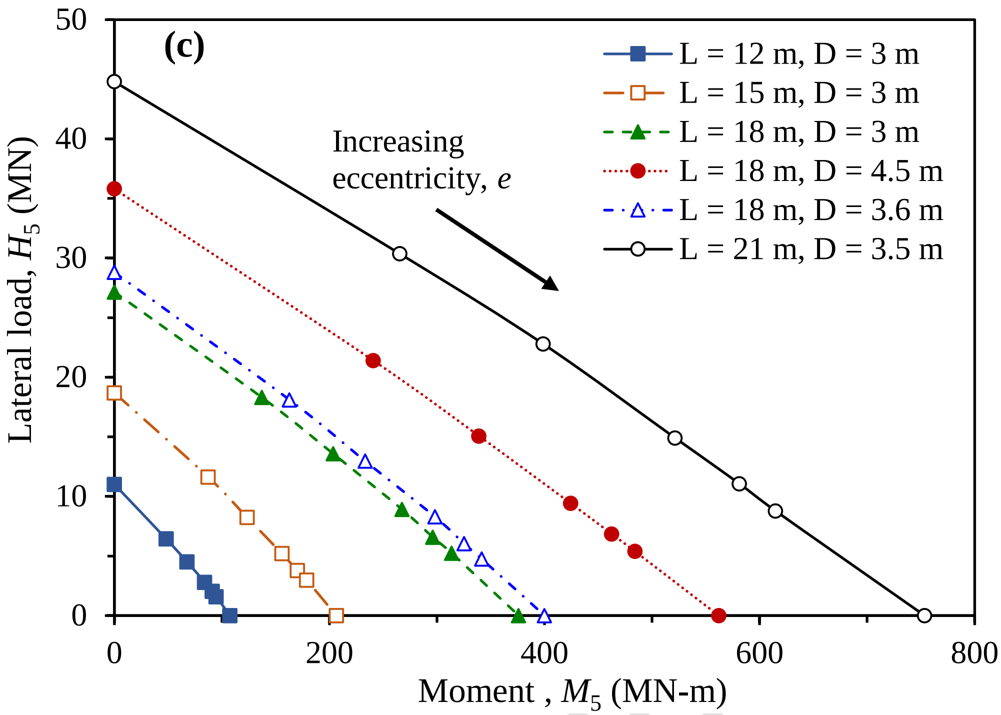

Fig. 9. Lateral load–moment interaction diagrams: (a) for θ = 0.5°, (b) for θ = 1°, (c) for θ = 5°

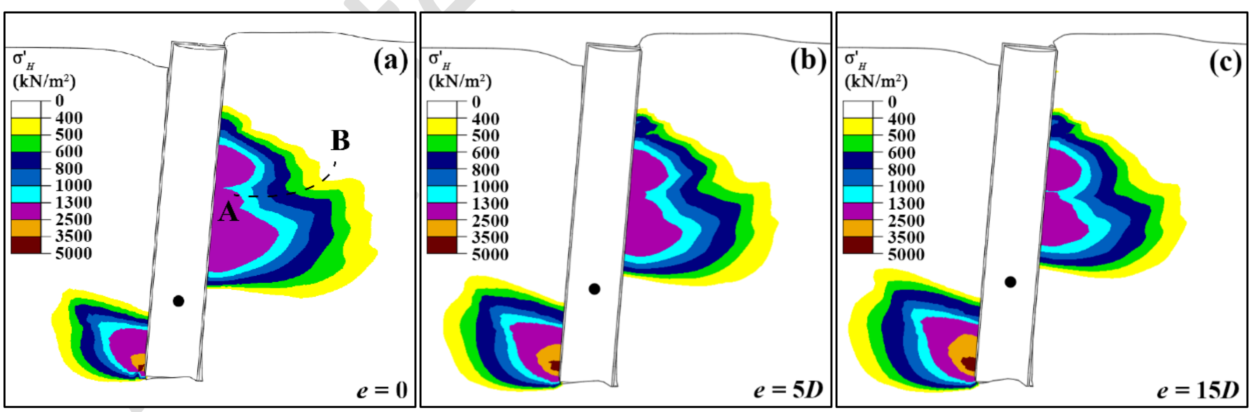

Fig. 10. Horizontal stress in soil at ultimate state ($\theta=5^0$) in the plane of symmetry

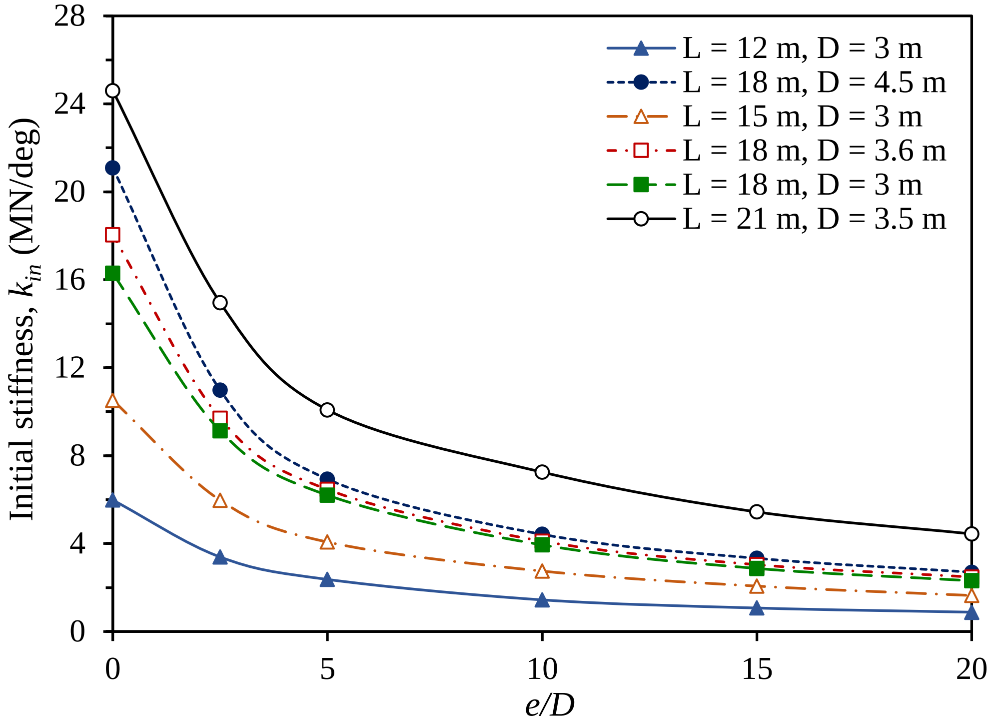

Fig. 11. Effects of length-to-diameter ratio and eccentricity on initial stiffness

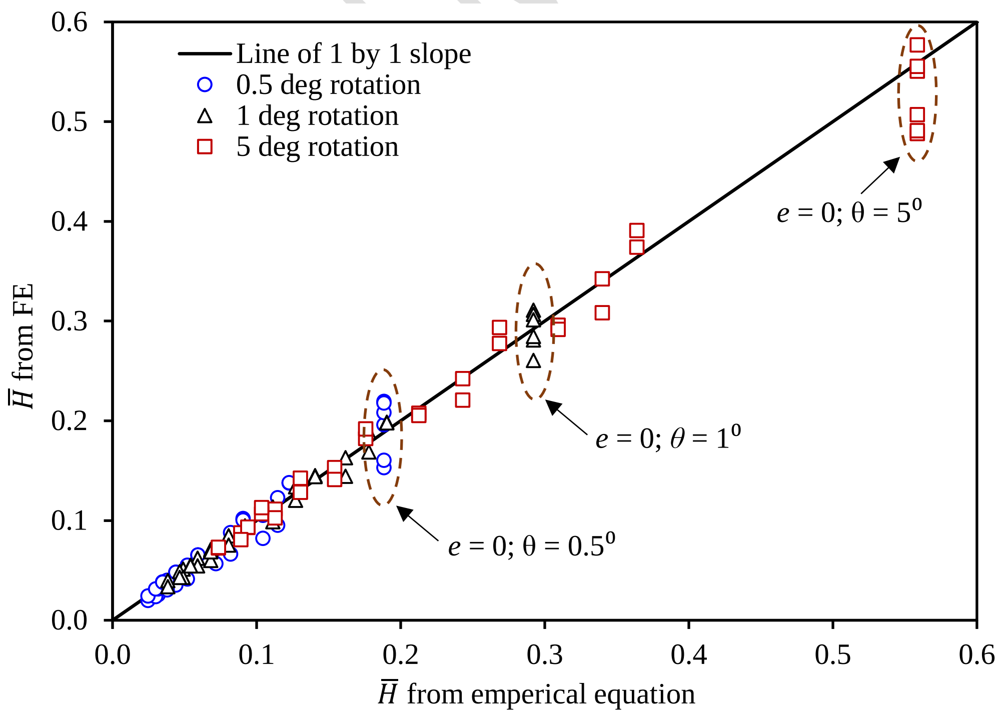

Fig. 12. Comparison between lateral loads calculated from proposed simplified equation and FE analyses

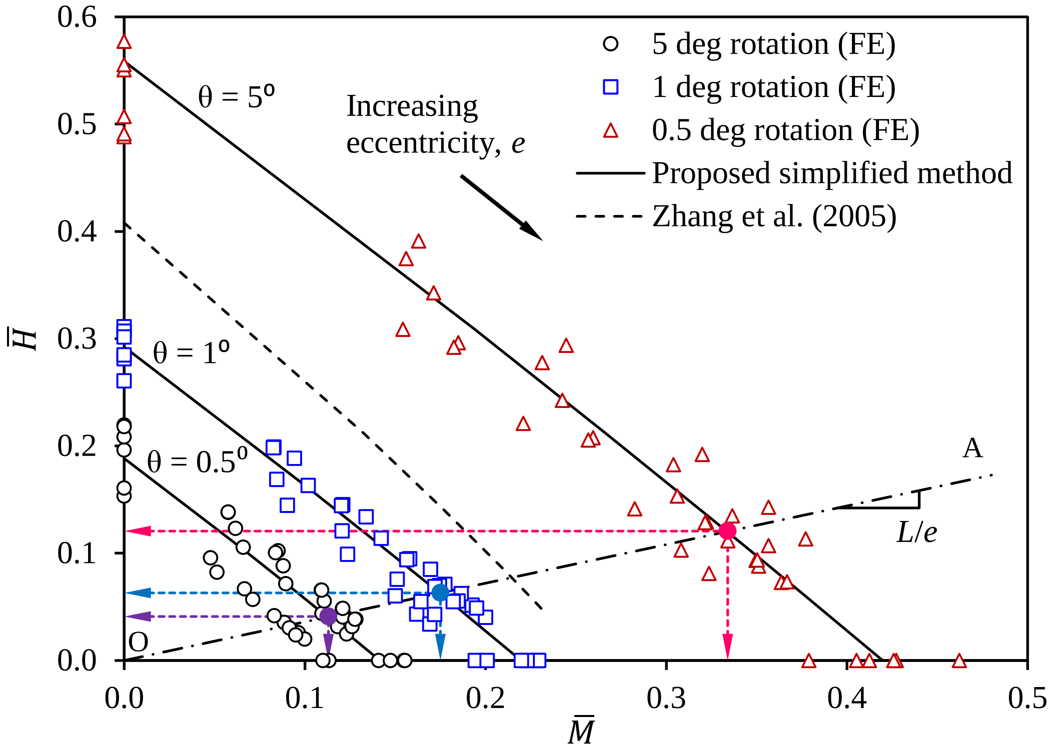

Fig. 13. Normalized force–moment interaction diagram for θ=0.5°, 1° and 5°